
A kinematic analysis of the CO clouds toward a reflection nebula NGC 2023 observed with the Nobeyama 45 m telescope; Further evidence for a cloud-cloud collision in the Orion region

Rin YAMADA¹, Rei ENOKIYA¹, Hidetoshi SANO^{1, 2}, Shinji FUJITA^{1, 3}, Mikito KOHNO^{1, 4}, Daichi TSUTSUMI¹, Atsushi NISHIMURA³, Kengo TACHIYAMA¹, and Yasuo FUKUI^{1, 5}

¹Department of Physics, Nagoya University, Furo-cho, Chikusa-ku, Nagoya 464-8601, Japan

²National Astronomical Observatory of Japan, National Institutes of Natural Sciences, 2-21-1 Osawa, Mitaka, Tokyo 181-8588, Japan

³Department of Physical Science, Graduate School of Science, Osaka Prefecture University, 1-1 Gakuen-cho, Naka-ku, Sakai, Osaka 599-8531, Japan

⁴Astronomy Section, Nagoya City Science Museum, 2-17-1 Sakae, Naka-ku, Nagoya, Aichi 460-0008, Japan

⁵Institute for Advanced Research, Nagoya University, Furo-cho, Chikusa-ku, Nagoya 464-8601, Japan

*E-mail: yamada@a.phys.nagoya-u.ac.jp

Received (reception date); Accepted (acceptation date)

Abstract

We have analyzed new CO($J = 1-0$) data in the region of a reflection nebula NGC 2023 with a particular focus on the detailed kinematical properties of the molecular gas. The results show that there are two velocity components which indicate signatures of dynamical interaction revealed at a high resolution of $19''$ ($= 0.04$ pc). Based on the results we propose a hypothesis that two clouds collided with each other and triggered the formation of the B1.5 star HD 37903 in addition to 20 lower mass stars in two small clusters with a size of 2 pc. Although the

previous study favored a scheme of triggering by the HII region (e.g., Mookerjea et al. 2009), the present results show that the effect of the HII region is limited only to the surface of the molecular cloud, and does not contribute to the gas compression and star formation. The present results lend support for the dominant role of cloud-cloud collision in forming high mass stars in addition to ~ 20 lower mass stars, which are also likely formed by the collision. The present case suggests all the high mass stars in the Orion region are formed by cloud-cloud collision.

Key words: ISM : clouds — ISM : kinematics and dynamics — ISM : Molecules — stars : formation

1 Introduction

The HII regions ionized by O or early B stars can compress the neutral gas by high pressure, which was first suggested by Oort (1954), and the role of HII regions in gas compression was studied into detail by Kahn (1955). The gas compression driven by HII regions was proposed by Elmegreen & Lada (1977) as a mechanism which triggers sequential formation of OB subgroups. A number of works were made along the line including the HII driven bubble like RCW 120 (Deharveng et al. 2005). Before that, Oort (1946) made another suggestion that the interstellar clouds are colliding often in the interstellar space based on optical absorption lines of a few discrete clouds moving at $10\text{--}15\text{ km s}^{-1}$, and the collision between clouds or cloud-cloud collision (CCC) may be an important process. This possibility was however not much followed until recently. Among the works of CCC on a various scale sizes (Torii et al. 2011, 2015, 2017; Fukui et al. 2014, 2015), Habe & Ohta (1992) and Inoue & Fukui (2013) presented theoretical works on CCC and showed that CCC is a viable mechanism to compress gas to trigger the formation of high-mass stars. Fukui et al. (2018) presented a methodology to identify CCC, where the following three features are used as observational signatures of CCC; i. two independent clouds having supersonic velocity separation are associated with high mass stars, ii. they show complementary distribution in space, and iii. they are linked by bridge features, which often show a V-shape in a position-velocity diagram. Until now more than 50 cases of CCC are found in the literature (see a compilation by Enokiya et al. 2019).

The Orion region is a unique site of active star formation within 400 pc of the sun, and serves as a precious site for studying star formation in detail, in particular, high-mass star formation. The most outstanding high-mass star cluster the Orion Nebula Cluster (ONC) in M42

is the best studied cluster in the Galaxy and the other high mass stars are distributed over 100 pc along the Galactic plane, which include M43, NGC 2024, NGC 2068, and NGC 2071 (see for a review of star formation Genzel & Stutzki 1989). According to the recent results, high-mass star formation triggered by CCC is shown in M42/M43 (Fukui et al. 2018), NGC 2068/NGC 2071 (Fujita et al. 2020), and NGC 2024 (Enokiya et al. 2020).

NGC 2023 is a reflection nebular in L1630, which is illuminated by an early B star HD 37903, and is separated by about 4 pc from the nearby HII region NGC 2024. Star formation in NGC 2023 has been extensively studied by a number of authors. Depoy et al. (1990) made JHK observations and identified 16 protostars at $1''.3$ resolution with 1.2 m telescope of Kitt Peak National Observatory. About a half of them are subject to the interstellar reddening, while the other half are subject to reddening due to disks or envelopes. Lada et al. (1991a) identified a cluster consisting of 21 members by a survey at 2.2 mm with the same instrument. A mm CS($J = 2-1$) survey at $1''.8$ resolution revealed five dense molecular cores LBS 34, 35, 36, 39, and 42 Lada et al. (1991b). Observations with the SEST 15 m telescope and IRAM 30 m telescope of the 1.3 mm continuum radiation at resolutions of $23''$ and $12''$, respectively, two sub-mm sources LBS36 SM1 and SM2 were discovered (Launhardt et al. 1996). Sandell et al. (1999) discovered molecular outflow whose velocity span is more than 200 km s^{-1} with a dynamical time scale of less than 3000 yr in observations of CO($J = 2-1$) and CO($J = 3-2$) emission at resolutions of $21''.5$ and $14'$, respectively, with the James Clerk Maxwell Telescope (JCMT), and called it NGC 2023 MM1. Another sub-mm source NGC 2023 MM2 was found to be associated with LBS36 SM2 by the same author. Johnstone et al. (2006) made a survey at $850 \mu\text{m}$ at $3''$ resolution and identified 23 sources in the region of NGC 2023 and the Horse Head Nebula. Mookerjea et al. (2009) identified 73 YSOs based on the data of *Spitzer* IRAC and MIPS and the $850 \mu\text{m}$ and $450 \mu\text{m}$ results of JCMT Submillimetre Common-User Bolometer Array. They made SED fitting and identified five sources to be Class 0. These observations also revealed a class I/0 associated with a sub-mm source NGC 2023 MM3 (Wyrowski et al. 2000) and that NGC2024 MM4 shows properties of a cold protostellar core. The authors also identified 10 class I/II sources, and 58 class II/III and class III sources. NGC 2023 is faced to an HII region IC 434 and the compression by the HII region was discussed as a trigger of star formation by Mookerjea et al. (2009).

The molecular clouds in NGC 2024 was studied by a number of authors (e.g., Meyer et al. 2008). Recently, Ripple et al. (2013) used the FCRAO 14m telescope to map the CO($J = 1-0$) emission in NGC 2023 with a $45''$ resolution. Nishimura et al. (2015) made an extensive large-scale study of the CO($J = 1-0$) and CO($J = 2-1$) emissions of ^{12}CO , ^{13}CO , and C^{18}O

obtained with the Osaka Prefecture University 1.85 m telescope and NANTEN, and revealed the detailed excitation states of CO. Most recently, the CO observations by Enokiya et al. (2020) were interpreted to show CCC as a trigger of O star formation. It is therefore interesting to explore the possible mechanism of triggering in NGC 2023 in order to have a comprehensive understanding of the L1630 region.

The aim of the present work is to make a detailed analysis of the CO cloud toward NGC 2023 and test what is the trigger of star formation. Nishimura et al. (2015) and Fukui et al. (2018) showed that the Orion region have multiple velocity components in a large scale. Enokiya et al. (2020) noted that the small velocity difference of $\sim 2 \text{ km s}^{-1}$ among these components requires a velocity resolution higher than 1 km s^{-1} . The NGC 2023 molecular cloud has not been observed at spatial high resolution better than $30''$ and with a high velocity resolution better than 1 km s^{-1} . The present study aims at revealing detailed kinematics of the molecular gas with the NRO 45 m telescope at $19''$ resolution and 0.3 km s^{-1} velocity resolution. The directions in the sky are given in the Galactic coordinates in the present paper. This paper is organized as follows. Section 2 describes the CO observations. Section 3 presents the results, and Section 4 discussion on star formation by triggering based on detailed study of cloud kinematics. Section 5 gives conclusions.

2 Observations

2.1 Observations by the Nobeyama 45-m telescope

We performed four molecular line observations including $^{12}\text{CO}(J = 1-0)$ and $^{13}\text{CO}(J = 1-0)$ line emission with 45-m telescope at the Nobeyama radio observatory in January 14, 2017 to 15, 2017 together with NGC 2024 observations (Enokiya et al. 2020). The half-power beam width is $14''$ at 115 GHz, and $15''$ at 100 GHz. We scanned $22' \times 26'$ area with OTF mapping mode. The map center was $(l, b) = (206.^\circ 86, -16.^\circ 53)$. To release scanning effect, we scanned l direction and b direction and adopted the RMS weighted average. The frontend was four-beam, dual-polarization, and two sideband (2SB) receiver named FOur-beam REceiver System on the 45-m Telescope Minamidani et al. (2016). The typical system noise temperatures including atmosphere were 180–270 K at 110 GHz and 150–250 K at 115 GHz in the stellar direction. The backend was SAM45, which is a FX type digital spectrometer kuno et al. (2011). SAM45 has 4096 channels with a bandwidth and resolution of 250 MHz and 61.04 kHz. These frequencies correspond to 650 km s^{-1} and 0.15 km s^{-1} , respectively, at 115 GHz. We checked the pointing accuracy before the observation by observing Ori-KL ($\alpha_{\text{J2000}}, \delta_{\text{J2000}} \sim (05^{\text{h}}35^{\text{m}}14.5,$

$-5^{\circ}22'30''.4$) with the 40 GHz HEMT receiver named H40. The pointing accuracy was better than $3''$. We used chopper wheel method to gain antenna temperature T_a^* (Kutner & Ulich 1981). We observed W3 as a standard source to fix the variation between the four beams in January 5, 2017 to January 7, 2017. The variation between the beams is lower than 20%. The main beam efficiency (η_{mb}) was 0.44 at 110 GHz and 0.43 at 115 GHz. We carried out two channel binning and convolution, and obtained the final data whose spectral and velocity resolution were $19''$ and 0.33 km s^{-1} . The typical rms noise level was 0.88 K at 110 GHz and 0.37 K at 115 GHz.

2.2 The other datasets

In the present paper, we used WISE archive data of $3.5 \mu\text{m}$, $4.5 \mu\text{m}$, and $22 \mu\text{m}$. The spectral resolution of WISE archive data are $6.4''$ ($3.5 \mu\text{m}$), $6.5''$ ($4.5 \mu\text{m}$), and $12''$ ($22 \mu\text{m}$).

3 Results

3.1 The distribution of CO gas

Figure 1 shows the total intensity distributions of $^{12}\text{CO}(J = 1-0)$ and $^{13}\text{CO}(J = 1-0)$. In Figure 1a $^{12}\text{CO}(J = 1-0)$ distribution has a peak at $(l, b) = (206^{\circ}85, -16^{\circ}55)$, where the exciting star HD 37903 of the reflection nebula and two dust condensations MM3/MM4 are located (Wyrowski et al. 2000; Mookerjee et al. 2009). The $^{13}\text{CO}(J = 1-0)$ cloud has two peaks at the $^{12}\text{CO}(J = 1-0)$ peak and another peak at $(l, b) = (206^{\circ}83, -16^{\circ}6)$, where MM1/MM2 and outflow are located. The $^{13}\text{CO}(J = 1-0)$ cloud is elongated nearly along the Galactic plane at 30 K km s^{-1} in Figure 1b, while it is tilted by 20 degrees to the Galactic plane. The 20 young stars shown by green points are distributed toward the two $^{13}\text{CO}(J = 1-0)$ peaks. We here define the $^{13}\text{CO}(J = 1-0)$ peaks as $^{13}\text{CO}(J = 1-0)$ peak1 toward $(l, b) = (206^{\circ}87, -16^{\circ}55)$ and $^{13}\text{CO}(J = 1-0)$ peak 2 toward $(l, b) = (206^{\circ}85, -16^{\circ}60)$. The both CO distributions show sharp intensity decrease toward the south. In $^{12}\text{CO}(J = 1-0)$, $^{13}\text{CO}(J = 1-0)$ peak 2 corresponding to the white cross is not seen probably because of self-absorption. We use the $^{13}\text{CO}(J = 1-0)$ emission in the following, which is not subject to self-absorption.

Figure 2 shows the velocity channel distribution of the $^{13}\text{CO}(J = 1-0)$ emission every 0.9 km s^{-1} in a velocity range from 8 km s^{-1} to 14 km s^{-1} . The peak 1 is found mainly in panel c, coinciding with the YSO distribution. We see a velocity gradient which show the eastern side is blue-shifted and the western side red-shifted. In panels c and d we see the elongation of the cloud at 20 degrees to the Galactic plane. This coincides with the velocity range of the CO

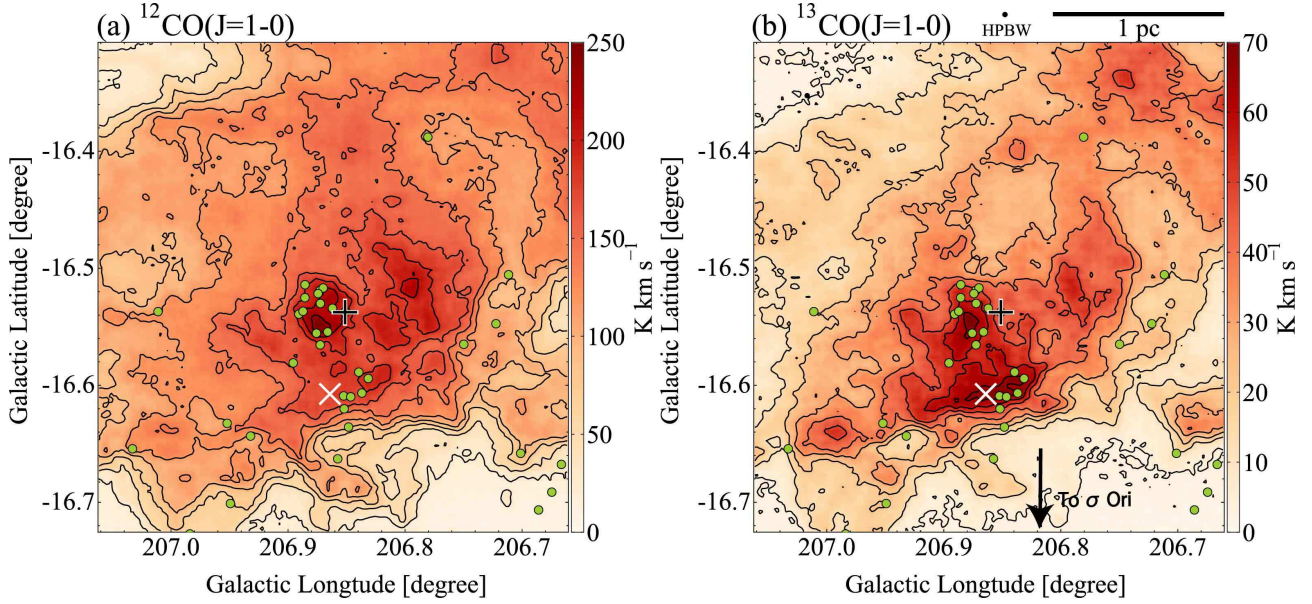


Fig. 1. (a) Integrated intensity map of $^{12}\text{CO}(J=1-0)$ obtained with NRO-45m. The integration velocity range is from 7.9 km s^{-1} to 13.9 km s^{-1} . The lowest contour and contour intervals are 23 K km s^{-1} ($\sim 15\sigma$). (b) Integrated intensity map of $^{13}\text{CO}(J=1-0)$. The integration velocity range is the same as (a). The lowest contour and contour intervals are 2.9 K km s^{-1} ($\sim 5\sigma$) and 8.7 K km s^{-1} ($\sim 15\sigma$), respectively. The black cross, white cross and green dots represent the positions of HD 37903, NGC 2023 MM1, and YSOs detected by Mookerjea et al. (2009).

component associated with the HII region IC 434 (Enokiya et al. 2020).

Figure 3 shows distributions of the 1st moment and 2nd moment of the $^{13}\text{CO}(J=1-0)$ emission. We see a clear trend that the cloud is blue-shifted in the east and is red-shifted in the west in addition to another red-shifted component at $(l, b) = (207^\circ 0, -16^\circ 7)$. The red-shifted gas shows an arc like distribution at $l = 206.65$ to 206.75 degree, and $b = -16.6$ to -16.4 degree. Within the intensity level above 30 K km s^{-1} , the 2nd moment is enhanced toward the region where the 1st moment is 11 km s^{-1} at $(l, b) = (206^\circ 8, -16^\circ 5)$, and another enhancement, while less obvious, is seen at $(l, b) = (206^\circ 93, -16^\circ 6)$. Figure 4 shows three CO profiles at the positions a, b, and c denoted in Figure 3, where we find the velocity peaks consistent with Figure 3. The profiles are peaked at 10 km s^{-1} at position a, and at 12 km s^{-1} at position c. The $^{13}\text{CO}(J=1-0)$ profile at position b shows two peaks at 10 km s^{-1} and 12 km s^{-1} , which are not clear in $^{12}\text{CO}(J=1-0)$. This indicates that $^{12}\text{CO}(J=1-0)$ is partially saturated due to high optical depth. The 5 km s^{-1} cloud is unrelated with the present cloud and is not discussed further (Enokiya et al. 2020).

The above results show that there are two velocity components in the NGC 2023 region. Enokiya et al. (2020) pointed out that the two clouds are mostly merged in NGC 2023, while they are resolved into two at 10 km s^{-1} and 13 km s^{-1} at some places. This is consistent with the present results. We adopt the velocity ranges based on the moment method used by

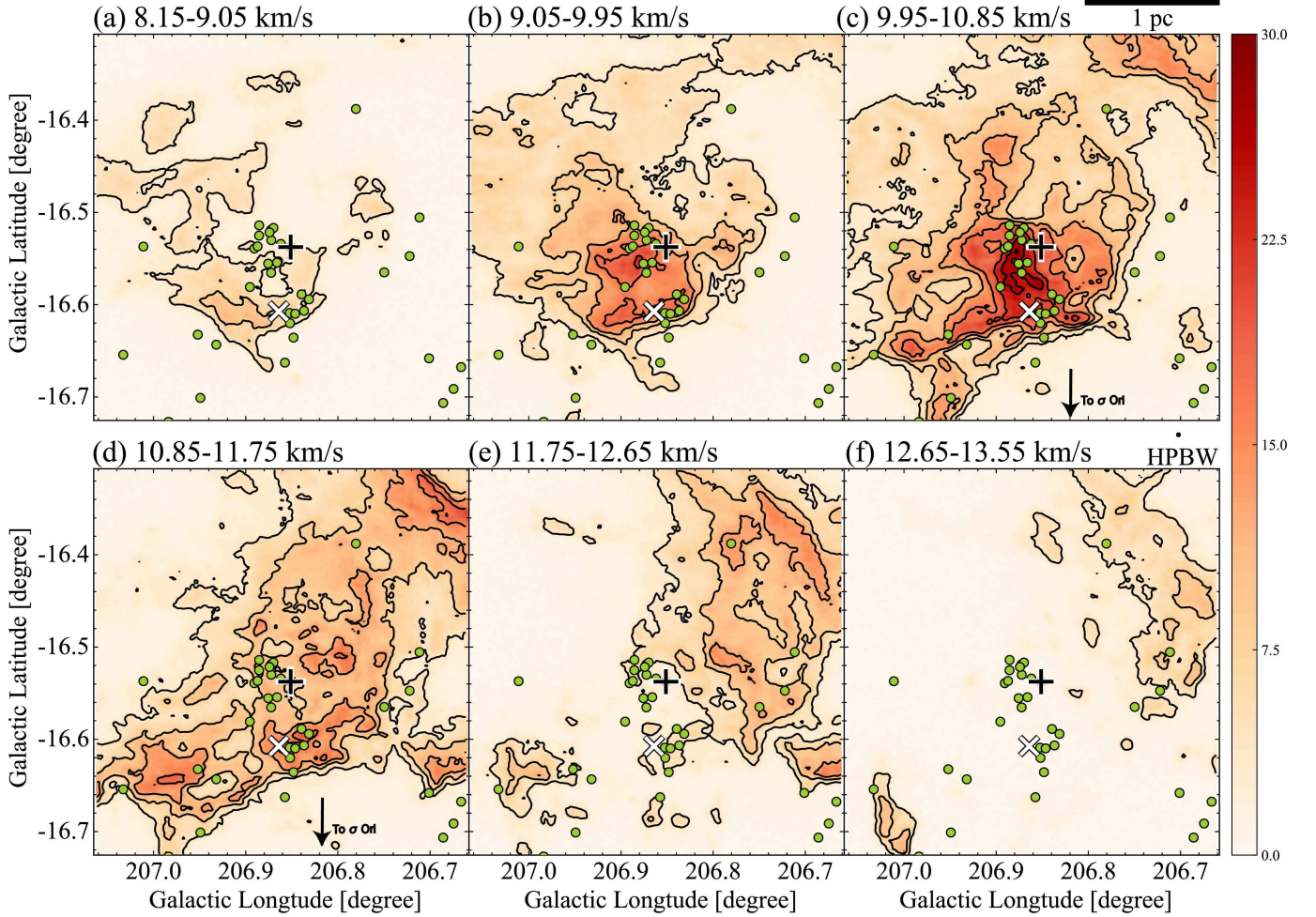


Fig. 2. Velocity channel maps of $^{13}\text{CO}(J = 1-0)$ toward NGC 2023. Each panel shows a $^{13}\text{CO}(J = 1-0)$ intensity map integrated over the velocity range from 8.15 to 13.55 km s^{-1} every 1.2 km s^{-1} . The black cross, white cross and green dots represent the positions of HD 37903, NGC 2023 MM1 and YSOs detected by Mookerjee et al. (2009), respectively. The lowest contour and contour intervals are 3.9 K km s^{-1} ($\sim 15\sigma$).

Enokiya et al. (2020) for the the blue-shifted cloud (the blue cloud) and red-shifted cloud (the red cloud). The 1st moment map in Figure 3 was used to separate the area with less than 10 km s^{-1} and that more than 12 km s^{-1} , and the average values of the first moment and the second moment are calculated. The mean velocity and velocity dispersion are then calculated. The upper bound of the blue cloud and the lower bound of the red cloud are about 10.85 km s^{-1} , corresponding to the dip between the two peaks in the $^{13}\text{CO}(J = 1-0)$ profile in Figure 4b. Further, in Figure 2 the cloud distribution changes significantly at around the velocity. We define 10.85 km s^{-1} as the boundary between the blue cloud and the red cloud.

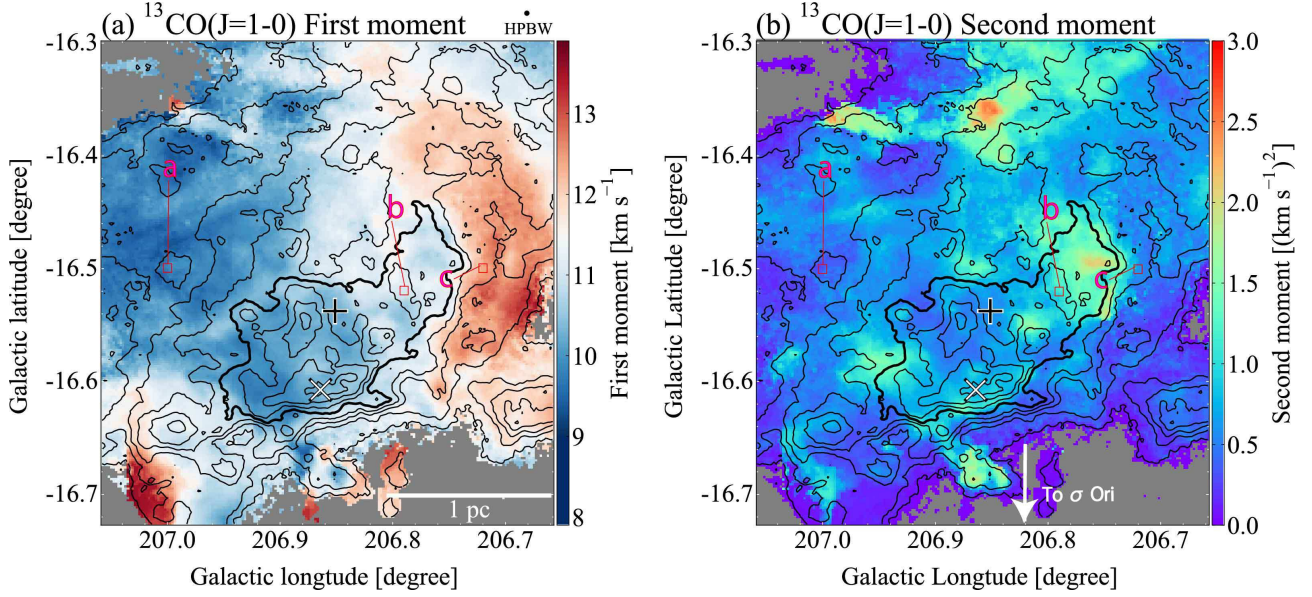


Fig. 3. First moment map (a) and second moment map (b) of $^{13}\text{CO}(J=1-0)$ in the velocity range of $7.9\text{--}13.9\text{ km s}^{-1}$ superposed on the $^{13}\text{CO}(J=1-0)$ integrated intensity contour as shown in the Figure 1b. The lowest contour and contour intervals are the same as Figure 1b. The black and white cross represent the positions of HD 37903 and NGC 2023 MM1, respectively. Black dots a–c in each map show the locations of the CO spectra in Figure 4.

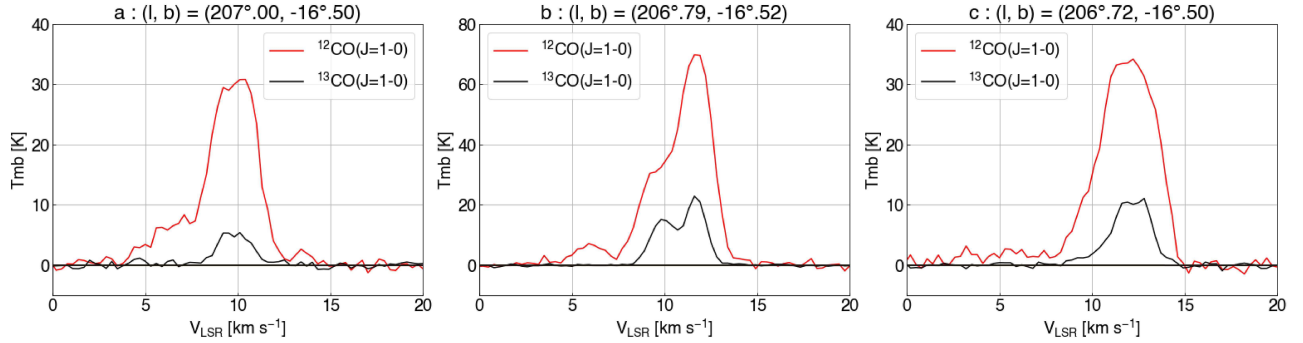


Fig. 4. CO spectra at the positions of the dots a–c in Figure 3. $^{12}\text{CO}(J=1-0)$ and $^{13}\text{CO}(J=1-0)$ are plotted in black and red, respectively.

3.2 Complementary distribution between the blue-shifted and red-shifted clouds

Figure 5a shows an overlay of the two velocity components at 10 km s^{-1} and 12 km s^{-1} , where the two components show complementary distribution. Figures 5b and 5c show position-velocity diagrams along the two straight lines in Figure 5a. The lines were adopted so as to include the two red-shifted components on the east and west as well as the position close to the stellar cluster including the B star. In the two diagrams we find a velocity distribution with a V-shape. The velocity variation which is consistent with that in Figure 5a is seen. We find a hint that the linewidths are enhanced toward the two positions between the two velocity components at offset $X = \pm 0.1$ degrees, which are consistent with the enhanced 2nd moment in Figure 5d. Table 1 lists the physical parameters of the two clouds, average column density $N(\text{H}_2)$, the

cloud mass M and the velocity range. The column density $N(\text{H}_2)$ is calculated by using the CO-to- H_2 conversion factor (X_{CO}) as follows;

$$N_{\text{H}_2} = W(\text{CO})X_{\text{CO}}, \quad (1)$$

where $W(\text{CO})$ (K km s^{-1}) is the integrated intensity of the CO emission. The molecular mass is given by equation (2),

$$M = m_{\text{H}}\mu D^2\Omega \sum_i N_i(\text{H}_2), \quad (2)$$

where m_{H} is the mass of hydrogen molecule, μ is the mean molecular weight, D distance to NGC2023 410 pc (Menten et al. 2007), Ω the solid angle of a pixel, and $N(\text{H}_2)$ the column density in eq. (1). The CO-to- H_2 conversion factor X_{CO} is taken as $1.0 \times 10^{20} (\text{K km s}^{-1})^{-1} \text{cm}^{-2}$ (Okamoto et al. 2017), and only the pixels with $W(\text{CO})$ larger than 5σ are used. Although the $^{12}\text{CO}(J = 1-0)$ emission is self-absorbed locally, the positions with clear self-absorption are limited in area. We thus adopted the method.

Table 1. Column densities and masses of total cloud, blue cloud and red cloud.

Cloud Name	V_{LSR} (km s^{-1})	Column Density (cm^{-2})	Mass (M_{\odot})
(1)	(2)	(3)	(4)
Blue cloud	7.9 –10.8	1.6×10^{22}	6.0×10^2
Red cloud	10.8 –13.9	1.3×10^{22}	5.0×10^2
Total	7.9 –13.9	2.6×10^{22}	1.1×10^3

Note. — Col. (1): Cloud name. Cols. (2) The velocity range of each cloud in Local Standard of Rest coordinate. Cols. (3) The maximum molecular hydrogen column density $N(\text{H}_2)$ derived from the $^{12}\text{CO}(J = 1-0)$ integrated intensity and the CO-to- H_2 conversion factor (X_{CO}) of $1.0 \times 10^{20} (\text{K km s}^{-1})^{-1} \text{cm}^{-2}$ (Okamoto et al. 2017) Col. (4): Mass of the clouds derived using the equation (2). We used the integrated intensity higher than 5σ in calculation.

4 Discussion

4.1 A cloud-cloud collision scenario

Based on the results in Section 3 we frame a hypothesis that the NGC 2023 cloud consist of two clouds of projected velocity difference of 2 km s^{-1} . The clouds are likely colliding to trigger the

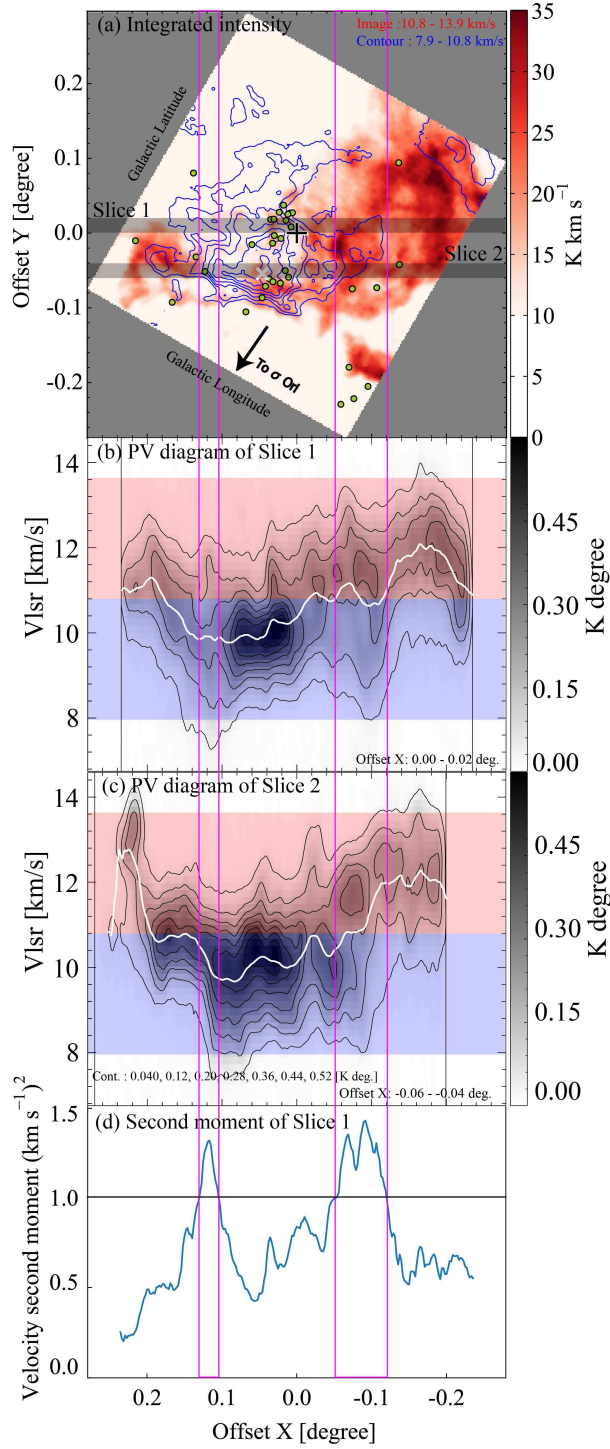


Fig. 5. (a) The $^{13}\text{CO}(J=1-0)$ distribution of red and blue clouds in the offset X–Y coordinates. The offset X–Y coordinate is defined by rotating the galactic coordinate clockwise by 30.00 degree. The rotation center is the position of HD 37903. The image shows the $^{13}\text{CO}(J=1-0)$ intensity integrated over the velocity range from 10.8–13.9 km s⁻¹. The blue contours show the intensity integrated over the range of 7.9–10.8 km s⁻¹. (b) The offset X–velocity diagram of the NGC 2023 region in $^{13}\text{CO}(J=1-0)$. Integration range in the offset Y is indicated as dark transparent belt superposed on the panel (a). The overlaid white line indicates velocity first moment in the same region as the offset X–velocity diagram averaged along the offset Y. (c) The graph presents the second moment in the same region as (b) averaged along the offset-Y. The vertical purple dotted line shows the region where the second moment in the (c) is larger than 1.0 (km s⁻¹)².

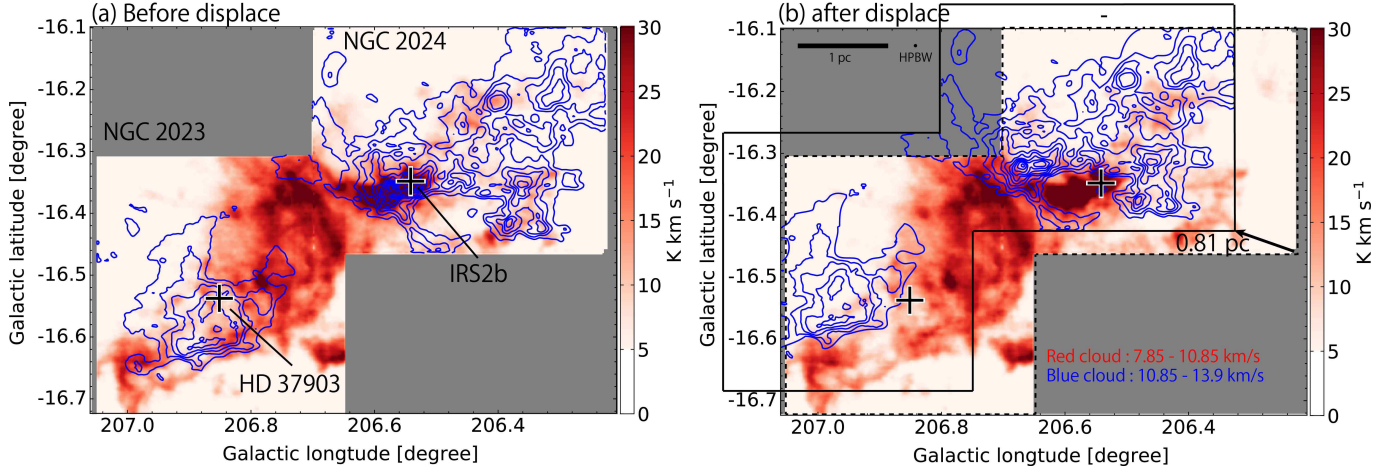


Fig. 6. (a) Integrated intensity covering NGC 2023 and NGC 2024 region in $^{13}\text{CO}(J = 1-0)$. Image shows the red shifted component of $10.85\text{--}13.9\text{ km s}^{-1}$. Overlaid con contour represent the distribution of blue-shifted component of $7.9\text{--}10.85\text{ km s}^{-1}$. (b) Integrated intensity distribution of red and blue components displaced for 0.81 pc .

formation of the B1.5 stars as well as the twenty YSOs in the two clusters. In the following, we describe details of the collisional process inferred from the present data and compares the results with the cloud-cloud collisions in the other regions, in particular, with the NGC 2024 cloud which seems to be connected to the present clouds (Meyer et al. 2008).

The two regions, NGC 2023 and NGC 2024 are connected as part of a large cloud extending to the north and the two velocity components are common properties in the NGC 2023 and NGC 2024 regions (for the whole view of the CO distribution see Nishimura et al. 2015). Figure 6 shows a combined $^{13}\text{CO}(J = 1-0)$ image of the NGC 2023 and NGC 2024 regions for the two velocity ranges of the colliding clouds taken with the 45 m telescope. A full account of the NGC 2024 region will be presented elsewhere (Enokiya et al. in preparation). Enokiya et al. (2020) showed that the two clouds in NGC 2024 have complementary distribution with each other with a displacement of 0.6 pc based on the $^{13}\text{CO}(J = 2-1)$ data taken with NANTEN2. We applied a displacement for the two regions in the same direction by assuming that the two clouds share common relative motion moving to east along the Galactic plane in a large scale in Figure 6b. Figure 6b shows the complementary distribution of 0.81 pc seems fairly good. The direction of the displacement explains that the site of star formation is on the western side of blue cloud in NGC 2023. The displacement is somewhat larger than in Enokiya et al. (2020) probably due to the higher resolution. So, the picture is that the whole parent clouds, both red-shifted and blue-shifted, extended by $\sim 10\text{ pc}$ are commonly triggering high mass star formation in the two interaction sites toward NGC 2024 and NGC 2023. We shall adopt the picture in the present paper, while the weakness of the CO emission in the northeast makes the

complementarity in NGC 2023 somewhat obscure as compared with NGC 2024. The collision time scale is roughly estimated to be 0.4 Myr from a ratio of $0.8 \text{ pc}/2 \text{ km s}^{-1}$ for an assumed angle of the collision direction to the line of sight of 45 degrees.

Star formation is taking place in the red cloud in NGC 2024 and in the blue cloud in NGC 2023. This suggests that density was higher in each cloud in the regions (Haworth et al. 2015). A marked difference is the number of high-mass stars between the two regions; more than ten high-mass stars in NGC 2024 and only one early B star in NGC 2023. This suggest that the column density in NGC 2024 was ten times higher in NGC 2024 than in NGC 2023 (see Figure 9 of Enokiya et al. 2020)

Enhancement of the 2nd moment is seen toward the two parts between the two clouds in Figure 5d. This is understood as caused by the enhanced turbulence in the collisional interface layers in the east and west of the blue-shifted cloud. The collision is able to compress gas according to the process as simulated by theoretical works (Habe & Ohta 1992; Inoue & Fukui 2013; Takahira et al. 2014; Shima et al. 2018). It is probable that the $^{13}\text{CO}(J = 1-0)$ core, having a size of $0.5 \text{ pc} \times 0.8 \text{ pc}$ was formed by the compression. The typical column density is $\sim 7 \times 10^{21} \text{ cm}^{-2}$ and the compressed mass is $\sim 100 M_{\odot}$, where B1.5 star and 20 YSOs were formed. The total stellar mass of these stars is estimated to be $\sim 30 M_{\odot} (= 10 M_{\odot} + 20 \times 1 M_{\odot})$, corresponding to a star formation efficiency of 30%. The YSOs may be still growing by mass accretion in the $^{13}\text{CO}(J = 1-0)$ core, while the B1.5 star has dispersed the ambient gas by its winds and created the cavity with the reflection nebula as discussed below. The elongation of the YSOs and the $^{13}\text{CO}(J = 1-0)$ core nearly vertical to the collision direction is consistent with collision nearly along the Galactic plane, which is similarly to the collision in NGC 2024 (Enokiya et al. 2020). We presume that the collision path of the blue-shifted cloud is somewhat tilted to the west, resulting stronger compression on the western edge of the blue shifted cloud. This also explains the arc shape of the red-shifted cloud as caused by the bow-shock by the collision.

4.2 The cavity toward HD 37903

Figure 7a shows an overlay of the $^{13}\text{CO}(J = 1-0)$ core with the infrared image taken with WISE, and Figure 7b shows a strip map of the infrared emission and the $^{13}\text{CO}(J = 1-0)$ intensity along the green line in Figure 7a. The infrared emission is the reflection light of the B1.5 star. The reflected light is asymmetric with respect to the star, which is probably due to the $^{13}\text{CO}(J = 1-0)$ gas distribution just after the collisional compression which had a peak

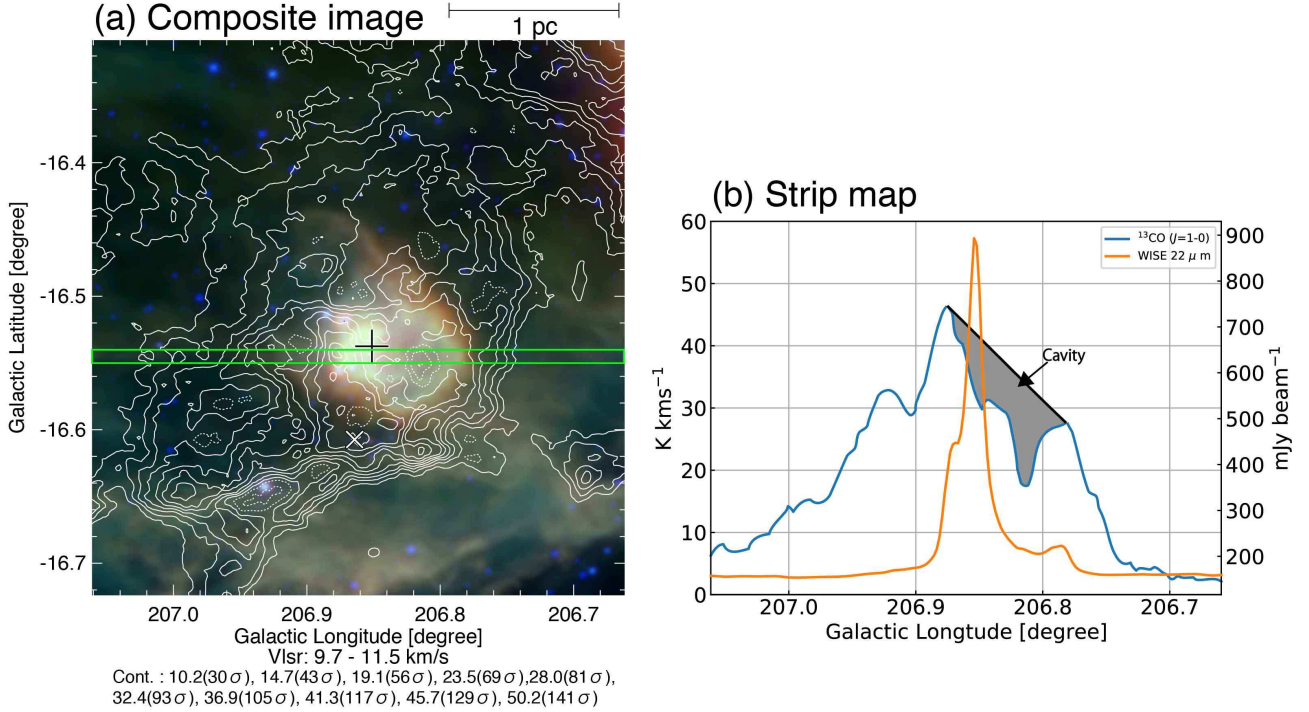


Fig. 7. (a) Three-color infrared image of NGC 2023 obtained with WISE. The red, green, and blue represent 22 μm , 12 μm , and 4.6 μm , respectively. Contours show total intensity of $^{13}\text{CO}(J = 1-0)$ with the velocity between 7.9 and 13.9 km s^{-1} . The black cross and white cross represent the positions of HD 37903 and NGC 2023 MM1, respectively. (b) Intensity of the $^{13}\text{CO}(J = 1-0)$ and 22 μm on the green line superposed on the panel (a).

toward $l = 206^\circ 87$ with density decrease toward the west. We speculate that the distribution caused the present asymmetric cavity with respect to the B1.5 star, and that the stellar winds pushed the gas more deeply into the western part with density decrease. It is probable that the initial density distribution is more enhanced toward the current cavity and part of the gas was removed by the winds at $l = 206^\circ 78-206^\circ 85$. If we assume the initial density of $3.0 \times 10^3 \text{ cm}^{-3}$ with a size of 0.7 pc the total mass dispersed is estimated to be $24 M_\odot$. So, currently the stellar feedback has a limited effect on the parent gas of $1000 M_\odot$ at a level of a few % in gas removal.

4.3 The effect of the HII region in star formation

It has been a concern if IC 434 in triggering star formation in NGC 2023 and NGC 2024 (e.g., Mookerjea et al. 2009). Figure 8 shows a latitude-velocity diagram taken along the line at $l = 206^\circ 85$ in Figure 8. This diagram shows the velocity distribution of the $^{13}\text{CO}(J = 1-0)$ gas vertical to the ionization front formed by the HII region. The previous paper suggested such interaction may trigger star formation in NGC 2023 (Mookerjea et al. 2009).

We find a strong intensity gradient toward σ Ori as is consistent with the effect of the

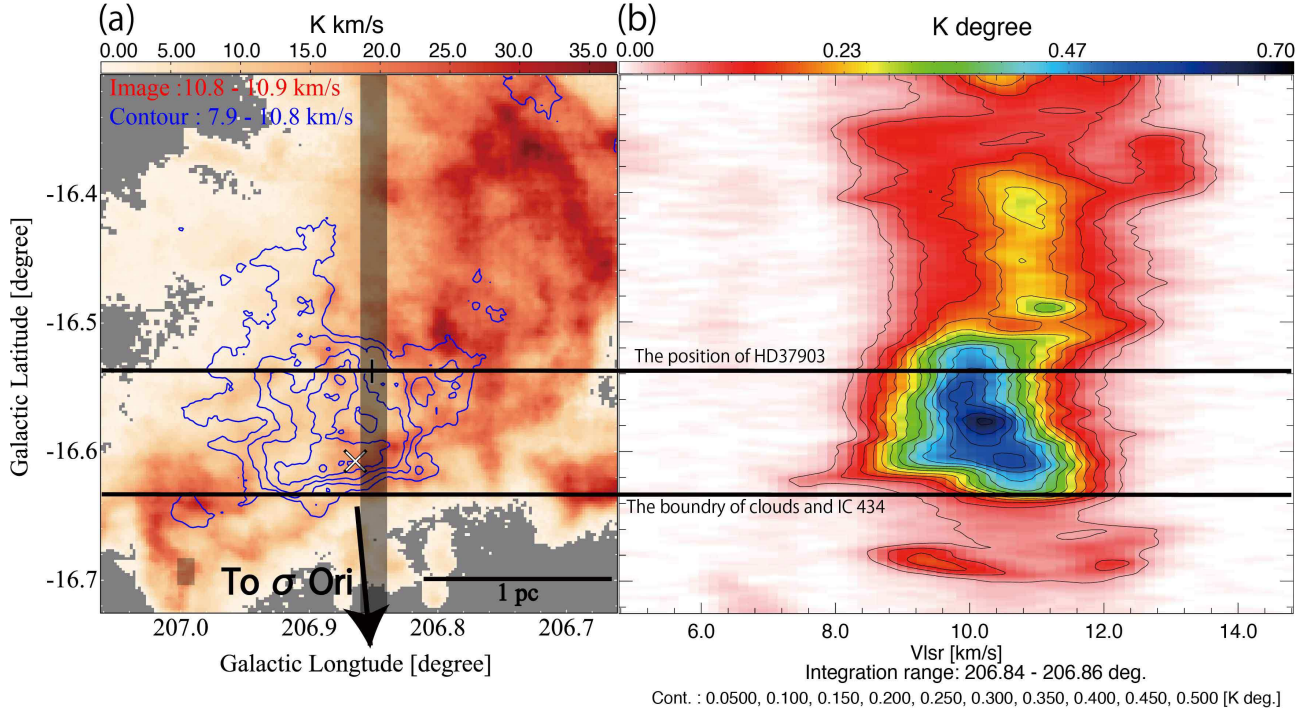


Fig. 8. (a) The $^{13}\text{CO}(J = 1-0)$ distribution of red and blue clouds. The image shows the $^{13}\text{CO}(J = 1-0)$ intensity integrated over the velocity range from $10.8-13.9 \text{ km s}^{-1}$. The blue contours show the intensity integrated over the range of $7.9-10.8 \text{ km s}^{-1}$. The dark transparent belt shows the integration range of the Galactic longitude–velocity diagram presented in (b) The black arrow indicates the direction of the σ Ori, which is the exciting star of the HII region IC 434. The upper and lower black vertical lines show the Galactic latitude of the exciting star HD 37903 and the boundary of molecular gas and the HII region.

ionization. In this region the boundary between IC 434 and the CO gas is seen as the optical emission nebula of HII gas, while the exact location of σ Ori is not known. It is possible that there is some velocity shift in the CO gas facing σ Ori if the gas is accelerated by the HII region. It is however not clear how the gas is accelerated by the ionization front, because no significant velocity shift is found at Galactic latitude above $-16^\circ 55$ in Figure 8. We see some hint of a velocity shift only at latitude below 16.6 degrees, where a small shift from 10 km s^{-1} to 11 km s^{-1} may exist in the $^{13}\text{CO}(J = 1-0)$ cloud. Most of the star forming $^{13}\text{CO}(J = 1-0)$ cloud, therefore, seems to be unaffected. It is also possible the small shift is due to the collisional acceleration with the red-shifted cloud in the south, where the remnant of the red-shifted cloud has been ionized significantly below $-16^\circ 63$. Consequently, we find no compelling evidence for the trigger of star formation by the HII region.

5 Conclusions

The region of NGC 2023 was studied by using the $^{12}\text{CO}(J = 1-0)$ and $^{13}\text{CO}(J = 1-0)$ data taken with the NRO 45 m telescope at $19''$ resolution. The data allowed us to reveal detailed gas kinematics at high spatial/velocity resolution of $0.04 \text{ pc} / 0.3 \text{ km s}^{-1}$ at a distance of 410 pc. We have successfully resolved the interacting two clouds and presented a scenario of CCC as a trigger of star formation in NGC 2023. The main conclusions are summarized below.

1. The cloud consists of two velocity components at 10 km s^{-1} and 12 km s^{-1} , and the two clouds show complementary distribution. The masses of the blue-shifted cloud and the red-shifted cloud are estimated to be $600 M_{\odot}$ and $500 M_{\odot}$, respectively, with a typical column density of $(5-6) \times 10^{21} \text{ cm}^{-2}$. We find broadening of the linewidth toward the two interfaces of the two clouds which is a possible signature of the dynamical interaction.
2. We present a hypothesis that the two clouds collided with each other and triggered the formation of a B1.5 star HD 37903 and twenty young stellar objects. The $^{13}\text{CO}(J = 1-0)$ core has $\sim 100 M_{\odot}$ and the star formation efficiency is estimated to be $\sim 30\%$. The gas column density of the core $5 \times 10^{21} \text{ cm}^{-2}$ is slightly below the empirical threshold for O star formation, and the formation of a B1.5 star is consistent with the threshold. This shows that cloud-cloud collision also triggers not only high mass stars but also the formation of low-mass stars. The time scale of the collision is estimated to be 0.2 Myr. This short time is consistent with the stellar age as well as that there is no displacement in the complementary distribution.
3. The NGC 2023 cloud having a size of roughly 2 pc is elongated nearly along the Galactic plane and is physically connected with the NGC 2024 cloud which is separated by 4 pc from each other. A comparison with the cloud-cloud collision in NGC 2024 (Enokiya et al. 2020) suggests that the collisions are taking in a similar manner with each other in terms of the collision direction nearly parallel to the plane.

Including the other regions in Orion where high star formation was triggered by cloud-cloud collision, M42/M43 (Fukui et al. 2018), NGC 2071/NGC 2069 (Fujita et al. 2020), and NGC 2024 (Enokiya et al. 2020), we infer that cloud-cloud collision triggered all the high-mass star formation in Orion A and B. We suggest that cloud-cloud collision provides a viable alternative to the sequential star formation scenario (Elmegreen & Lada 1977).

Acknowledgments

We are grateful to Akio Taniguchi, Kazuki Shiotani, Keisuke Sakasai, and Kenta Matsunaga for their valuable support during data analysis. We also acknowledge Hiroaki Yamamoto for useful discussion of this paper. The Nobeyama 45-m radio telescope is operated by Nobeyama Radio Observatory, a branch of National Astronomical Observatory of Japan. This publication makes use of data products from the Wide-field Infrared Survey Explorer, which is a joint project of the University of California, Los Angeles, and the Jet Propulsion Laboratory/California Institute of Technology, funded by the National Aeronautics and Space Administration. This study was financially supported by Grants-in-Aid for Scientific Research (KAKENHI) of the Japanese Society for the Promotion of Science (JSPS; grants No., 15H05694, 25287035, 19H05075, and 20H01945). H.S. was supported by “Building of Consortia for the Development of Human Resources in Science and Technology” of Ministry of Education, Culture, Sports, Science and Technology (MEXT; grant No. 01-M1-0305).

References

- Deharveng, L., Zavagno, A., & Caplan, J. 2005, *A&A*, 433, 565
- Depoy, D. L., Lada, E. A., Gatley, I., et al. 1990, *ApJL*, 356, L55
- Elmegreen, B. G., & Lada, C. J. 1977, *ApJ*, 214, 725
- Enokiya, R., Torii, K., & Fukui, Y. 2019, *PASJ*, doi:10.1093/pasj/psz119
- Enokiya, R., Ohama, A., Yamada, R., et al. 2020, arXiv e-prints, arXiv:1912.11607
- Fujita, S., Tsutsumi, D., Ohama, A., et al. 2020, *PASJ*, doi:10.1093/pasj/psaa005
- Fukui, Y., Ohama, A., Hanaoka, N., et al. 2014, *ApJ*, 780, 36
- Fukui, Y., Harada, R., Tokuda, K., et al. 2015, *ApJL*, 807, L4
- Fukui, Y., Torii, K., Hattori, Y., et al. 2018, *ApJ*, 859, 166
- Genzel, R., & Stutzki, J. 1989, *ARA&A*, 27, 41
- Habe, A., & Ohta, K. 1992, *PASJ*, 44, 203
- Haworth, T. J., Tasker, E. J., Fukui, Y., et al. 2015, *MNRAS*, 450, 10
- Inoue, T., & Fukui, Y. 2013, *ApJL*, 774, L31
- Johnstone, D., Matthews, H., & Mitchell, G. F. 2006, *ApJ*, 639, 259
- Kahn, F. D. 1955, *Gas Dynamics of Cosmic Clouds*, 115
- Kuno N., et al. 2011, in *Proc. 2011 XXXth URSI General Assembly and Scientific Symposium*, Vol. 1 (New York: IEEE), 3670
- Kutner, M. L., & Ulich, B. L. 1981, *ApJ*, 250, 341
- Lada, E. A., Bally, J., & Stark, A. A. 1991a, *ApJ*, 368, 432
- Lada, E. A., Depoy, D. L., Evans, N. J., et al. 1991b, *ApJ*, 371, 171
- Lada, C. J., & Lada, E. A. 1991, *The Formation and Evolution of Star Clusters*, 3
- Launhardt, R., Mezger, P. G., Haslam, C. G. T., et al. 1996, *A&A*, 312, 569
- Menten, K. M., Reid, M. J., Forbrich, J., et al. 2007, *A&A*, 474, 515
- Meyer, M. R., Flaherty, K., Levine, J. L., et al. 2008, *Handbook of Star Forming Regions, Volume I*, 662
- Minamidani, T., Nishimura, A., Miyamoto, Y., et al. 2016, *Proc. SPIE*, 99141Z
- Mookerjea, B., Sandell, G., Jarrett, T. H., et al. 2009, *A&A*, 507, 1485
- Nishimura, A., Tokuda, K., Kimura, K., et al. 2015, *ApJS*, 216, 18
- Okamoto, R., Yamamoto, H., Tachihara, K., et al. 2017, *ApJ*, 838, 132
- Oort, J. H. 1946, *MNRAS*, 106, 159
- Oort, J. H. 1954, *Bull. Astron. Inst. Netherlands*, 12, 177
- Ripple, F., Heyer, M. H., Gutermuth, R., et al. 2013, *MNRAS*, 431, 1296

Sandell, G., Avery, L. W., Baas, F., et al. 1999, ApJ, 519, 236
Shima, K., Tasker, E. J., Federrath, C., et al. 2018, PASJ, 70, S54
Takahira, K., Tasker, E. J., & Habe, A. 2014, ApJ, 792, 63
Torii, K., Enokiya, R., Sano, H., et al. 2011, ApJ, 738, 46
Torii, K., Hasegawa, K., Hattori, Y., et al. 2015, ApJ, 806, 7
Torii, K., Hattori, Y., Hasegawa, K., et al. 2017, ApJ, 835, 142
Ulich, B. L., & Haas, R. W. 1976, ApJS, 30, 247
Wyrowski, F., Walmsley, C. M., Goss, W. M., et al. 2000, ApJ, 543, 245
Zari, E., Brown, A. G. A., de Bruijne, J., et al. 2017, A&A, 608, A148